β-FeOOH/TiO₂/cellulose nanocomposite aerogel as a novel heterogeneous photocatalyst for highly efficient photo-Fenton degradation

Jun Jing, [ID] Yucheng Feng, Shuying Wu, Zhangjie Ye, Liu Yang, Jiaolong Li, Youyan Chen and Fei Yang*

The photo-Fenton reaction provides an effective strategy for the removal of organic pollution in water environments. However, it remains a great challenge to develop photo-Fenton catalysts with high photocatalytic activity, low catalyst losses and excellent recyclability. In this work, a β-FeOOH/TiO₂/cellulose nanocomposite aerogel was fabricated as an efficient and convenient heterogeneous catalyst in the photo-Fenton system *via in situ* synthesis of TiO₂ and β-FeOOH NPs on a cellulose-based aerogel. The cellulose aerogel not only acted as a microreactor to prevent aggregation of particles, but also acted as a supporting material to improve the stability and reusable performance of the catalyst. Meanwhile, the synergy between TiO₂ and β-FeOOH endowed the cellulose-based nanocomposite aerogel with highly efficient photo-Fenton degradation of dyes. As a result, the composite β-FeOOH/TiO₂/cellulose aerogel displayed high photocatalytic performance. Its removal efficiency of MB reached 97.2% under weak UV light for 65 min. There is no obvious decrease in the catalytic efficiency after 5 cycles, suggesting the stability and recyclability of the composite aerogel. This study provides a novel strategy for the preparation of efficient green heterogeneous catalysts by using renewable resources, and shows composite catalyst processes have great potential in wastewater treatment.

1. Introduction

Among a large number of environment pollution problems, water contamination is one of the most serious forms, which is an increasingly significant threat to human health.[1,2] Therefore, it is necessary to develop effective and environmentally friendly water purification methods. There are several conventional treatment methods, such as biodegradation, adsorption, filtration, flocculation and chemical oxidation.[3–5] Compared with as-mentioned methods, one of the advanced oxidation processes (APOs), the Fenton reaction has received considerable attention due to its capability to produce more hydroxyl radicals and completely degrade refractory organic pollutants. However, the conventional Fenton reaction has some shortcomings such as difficulty of recovering and reusing the catalyst, by-product of a large amount of iron sludge and low utilization efficiency of hydrogen peroxide.[6,7] Therefore, developing Fenton-like catalysts with excellent recyclability and stability, superior catalytic properties, and high specific surface area that are green is important.

Recently, there has been growing interest in heterogeneous photo-Fenton catalysis. Akaganeite (β-FeOOH), an iron oxide-hydroxide, has been considered as a promising iron-based heterogeneous photo-Fenton catalyst because of its photo-catalytic activity, low cost, low toxicity and environmentally friendly properties.[8–10] Furthermore, it can be convenient to be coupled with other components because of the abundant hydroxyl groups on the surface. However, the degradation efficiency of FeOOH has been greatly limited by the slow cycle efficiency of Fe(II)/Fe(III) and the limited exposed active sites. Previous research has established that combination of iron-based catalyst and semiconductor material is an effective strategy to enhance the photocatalytic performance.[11–13] The photoexcited electrons of semiconductor transport to iron-based catalyst under irradiation, which can not only reduce the electron–hole recombination of semiconductor, but also accelerate the transformation between Fe(III) and Fe(II). Thus, FeOOH combined with some semiconductors such as TiO₂, CdS and WO₃ has provided a synergistic degradation to generate more active radicals and improve the efficiency of photo-Fenton reaction.[14,15] Nevertheless, the composite catalyst particles have a tendency to aggregate to larger particle that leads to decrease the effective surface area. Besides, the recovery of catalyst particle from treated water is generally high cost and problematic. Therefore, immobilizing catalyst particle onto supporting materials is the ideal resolution to improve the stability and reusable performance of the supported catalyst.

The matrix is generally considered to play an important role in catalysts design. Therefore, it is essential to select materials

State Key Laboratory of Pulp and Paper Engineering, South China University of Technology, Guangzhou 510640, China. E-mail: yangfei@scut.edu.cn

with special structures as the matrix.[16] Aerogel, a three-dimensional hierarchical microstructure and porous network, is a porous material with unique properties, such as extremely low density, high porosity, large active surface area.[17,18] Inheriting the common features of aerogels with additional advantages of renewability, biocompatibility, easy modification, inexpensive and renewable raw materials, cellulose aerogels are promising candidates for photocatalytic applications.[19–21] In particular, the plenty of hydroxyl groups in the cellulose chains provide effective binding sites for catalyst particles. In the *in situ* strategy, the precursors are preloaded on cellulose aerogel and then converted to nanoparticles.[22] During this process, cellulose aerogel acted as a microreactor to prevent particles agglomeration and disperse particles evenly. Based on previously reports, it is feasible to load particles onto cellulose aerogel by *in situ* synthesis.

Herein, we propose a novel strategy to fabricate multi-component synergetic photocatalyst based on β-FeOOH/TiO$_2$ supported on 3D cellulose aerogel. TiO$_2$ as photocatalyst was grown *in situ* on precursor of cellulose hydrogel and then β-FeOOH NPs as Fenton catalyst were synthesized and fastened *in situ* on the composited gel. Compared with single photocatalyst or Fenton catalyst, the unique structural and functional properties of the different components endowed the as-prepared cellulose-based nanocomposite aerogel with highly efficient photo-Fenton degradation of dyes. This work demonstrates the potential of β-FeOOH/TiO$_2$/cellulose nanocomposite aerogel in photo-Fenton reactions for environmental treatment.

2. Experimental section

2.1 Materials

The cotton pulp was supplied by Fengyuan Special Paper Co., Ltd. (Xingtai, China). Sodium hydroxide, urea, iron(III) chloride hexahydrate, tetrabutyl titanate (TBT), epichlorohydrin (ECH), *tert*-butanol (TBA), triethanolamine (TEOA) and Benzoquinone (BQ) were provided from Guangdong Guanghua Sci-Tech Co., Ltd. (Guangzhou, China). All chemical reagents were analytical grade and without further purification. And all solutions were prepared with deionized water.

2.2 Fabrication of TiO$_2$/β-FeOOH composite aerogel

Cellulose was dissolved in 8 wt% NaOH/12 wt% urea solvent system that was precooled to −12 °C to form a 2 wt% cellulose solution. Then, 0.9 g of TBT was added into cellulose solution (30 g) with stirred for 30 min. After that, 2 mL ECH was added into the composite solution with stirring for 30 min. The above mixtures were poured into glass mold (r = 9 cm) and kept in a water bath at 60 °C for an hour to obtain TiO$_2$/cellulose composite hydrogels (CT). In addition, pure cellulose hydrogel (CA) was prepared. The composite hydrogels were immersed in deionized water that was replaced three times a day for two days.

For the preparation of TiO$_2$/β-FeOOH composite hydrogels, CT was immersed in 100 g 0.1 M FeCl$_3$ solution at 60 °C for 6 h, 9 h, 12 h, which were named as CTA-6, CTA-9, CTA-12,

respectively. In addition, a "CA-9" sample was prepared as a control sample, which is pure cellulose hydrogel was immersed in 100 g 0.1 M FeCl$_3$ solution at 60 °C for 9 h. Finally, the obtained composite hydrogels were immersed in the deionized water to remove FeCl$_3$ and then subjected to a freeze-drying process for 48 h at −30 °C in vacuum, and the following CTA aerogels were fabricated.

2.3 Characterizations

To analyze the chemical composition of composite aerogels, the materials were characterized by infrared spectroscopy (FTIR) using Nicolet Nexus-670 (Nicolet Instrument Technologies, USA) over a scan range of 400–4000 cm^{-1}. The X-ray diffraction (XRD) patterns were recorded in the 2θ range of 10–90° by X-ray diffractometer (X'Pert Powder, Panalytical, Netherlands) with a Cu-Kα radiation. The scanning electron microscope (SEM) images and energy dispersive spectroscopy (EDS) mappings were collected by the field emission scanning electron microscope (SU5000, Hitachi High-Tech, Japan) equipped with energy dispersive X-ray spectroscopy. Transmission electron microscopy (TEM) images were obtained using a JEOL JEM 2100 (Jeol, Japan). The X-ray photoelectron spectroscopy spectrums were detected by Axis Supra+ X-ray photoelectron spectrometer (Kratos Analytical, UK). The thermogravimetric analyses (TGA) were performed on a thermogravimetric analyzer (TG209F3, NETZSCH, Germany) at a heating rate of 10 °C min^{-1} from 40 to 800 °C under flowing nitrogen atmosphere. UV-vis absorption of the solutions was measured with UV-vis spectrophotometer (UV-1900, Shimadzu, Japan). UV-vis diffuse reflectance spectra (DRS) were obtained using a UV-vis spectrophotometer (UV-2700, Shimadzu, Japan) equipped with an integration sphere.

2.4 Photocatalytic degradation of MB in aqueous solution

The photocatalytic activity was evaluated in terms of the degradation rate of MB in an aqueous solution with 100 mL of 20 mg L^{-1}. An array of lamps (6 W × 3) with the wavelength of 254 nm was used as the weak UV light source, which was positioned 15 cm away from the solution. Typically, the samples (1.0 g L^{-1}) were stirred in the dark for 30 min to establish the adsorption–desorption equilibrium. Prior to irradiation, hydrochloric acid was used to regulate the pH of the solution, and H$_2$O$_2$ was added into the solution. The concentrations of MB solutions were measured by recording UV absorbance intensity at 664 nm with an UV-vis spectrophotometer at given time intervals. The formula used to calculate the degradation rate of MB is as follows:

$$D\ (\%) = (1 - C_t/C_0) \times 100\%$$

where D (%) is degradation rate of MB at time t, C_t (mg L^{-1}) is the MB concentration at time t and C_0 (mg L^{-1}) is the initial MB concentration, respectively.

And the photo-Fenton degradation kinetic was investigated with the pseudo-first-order kinetic model according to the following equation:

$$\ln(C_0/C) = kt$$

where k is the degradation rate constant (min^{-1}), t corresponds to the irradiation time, C_0 and C are the MB concentrations at 0 min and t min, respectively.

3. Results and discussion

3.1 Morphology and structure analysis

As shown in Fig. 1, the synthesis strategy applied for β-FeOOH/TiO$_2$/cellulose nanocomposite aerogel. First, TBT was added into cellulose solution as a TiO$_2$ precursor, and TBT was hydrolyzed in the NaOH/urea aqueous system, then TiO$_2$/cellulose hydrogels (CT) were fabricated. Second, CT were soaked in FeCl$_3$ solution, Fe^{3+} interacted with the polar hydroxyl groups of cellulose. Then β-FeOOH NPs were *in situ* synthesized in CT through the hydrolysis of FeCl$_3$. The abundant hydroxyl groups of cellulose were utilized as active site for *in situ* synthesis of TiO$_2$ and β-FeOOH, which prevent particle agglomeration and increase the effective surface area of catalyst. In this way, TiO$_2$ and β-FeOOH NPs were well dispersed on the cellulose aerogels. And the thorough contact between TiO$_2$ and β-FeOOH promotes the synergistic effect, enhancing the photo-Fenton degradation activity of CTA.
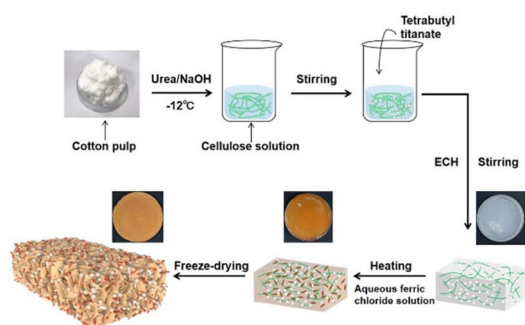

Fig. 1 Schematic diagram for preparation process of β-FeOOH/TiO$_2$/cellulose nanocomposite aerogel.

FTIR spectra of aerogel samples are depicted in Fig. 2a. Obviously, all spectra display the characteristic absorption band of cellulose. The band centred at around 3293 cm^{-1} is assigned to the stretching vibration of hydroxyl group, which shifted to lower wavenumbers after the incorporation of TiO$_2$ into cellulose aerogel, due to the hydrogen bonding interaction between cellulose and TiO$_2$. The signal at 2887 cm^{-1} and 1030 cm^{-1} is attributed to the stretching vibration of C–H bond and –C–O– group of secondary alcohols. The peak at 1650 cm^{-1} is corresponding to C=O stretching vibration of terminal aldehyde groups of cellulose structure.[20,23] For CTA-9, the peak at 896 cm^{-1} can be contributed to Fe–OH bending vibrations, and the band at 690 cm^{-1} and 475 cm^{-1} is attributed to Fe–O and Fe–OH stretching or lattice vibrations.[24,25] These results revealed that β-FeOOH incorporated into the cellulose aerogels.

The X-ray diffraction pattern of CA (Fig. 2b) shows two distinct peaks at $2\theta = 11.76°$ and 20.09°, corresponding to (1$\bar{1}$0) and (110) planes of cellulose II crystal. Compared to CA, the XRD pattern of CT was small and indistinct peaks except one obvious peak, implying amorphous TiO$_2$ was *in situ* synthesized at cellulose aerogels. For CTA-9, significant diffraction curves at 2θ of 11.87°, 16.82°, 26.74°, 35.19°, 39.24°, 46.45° and 55.90° corresponded to the (110), (200), (310), (211), (301), (411) and (521) crystal planes of β-FeOOH (PDF #43-1266), respectively, which further confirmed β-FeOOH had been successfully loaded into cellulose aerogels.

The chemical composition and bonding of the samples were further analyzed by XPS. The fully scanned spectrum (Fig. 3a) indicates the presence of C, O, Fe and Ti elements in the composite aerogel. There were three peaks (Fig. 3b) at 284.8, 286.5 and 288 eV in the C 1s spectrum, which were attributed to C–C, C–O, C=O from cellulose. In the Fe 2p spectrum (Fig. 3c), double peaks at 712.1 and 725.8 eV corresponded to the Fe^{3+} 2p$_{3/2}$ and Fe^{3+} 2p$_{1/2}$, while the two peaks at 710.6 and 724.1 eV were attributed to Fe^{2+} 2p$_{3/2}$ and Fe^{2+} 2p$_{1/2}$, respectively, confirming the existence of β-FeOOH. Owing to the presence of oxygen vacancies, Fe^{2+} was formed to maintain charge balance in the material. Two main peaks at 458.5 and 464.2 eV detected in Ti 2p spectrum (Fig. 3d) were referred to Ti^{4+} 2p$_{3/2}$ and Ti^{4+}
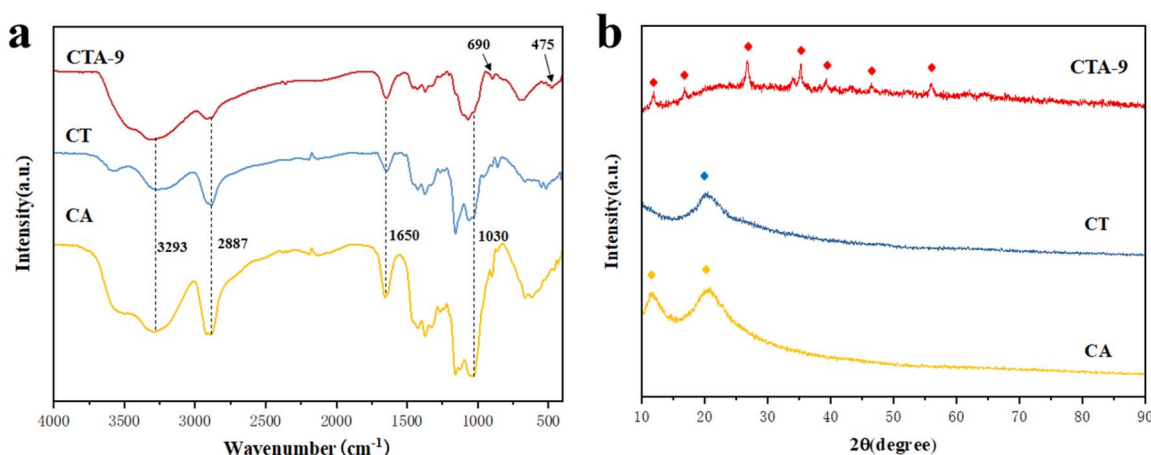

Fig. 2 Fourier transform infrared spectra (a), X-ray diffraction patterns (b) of the CA, CT, CAT-9.
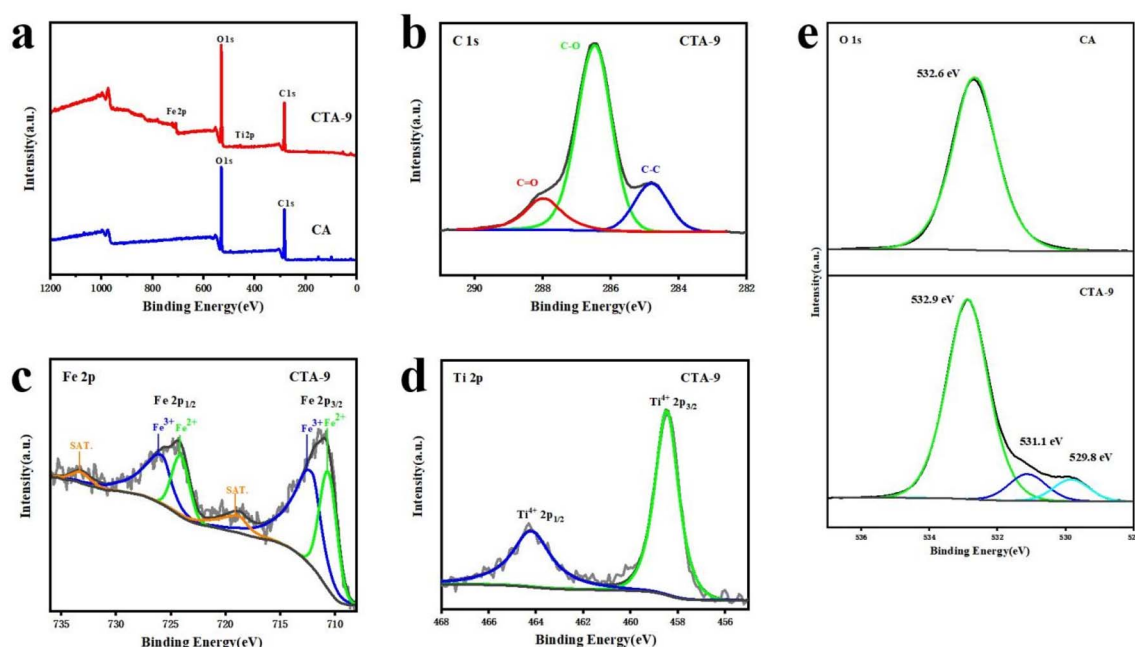
Paper

Fig. 3 XPS spectra (a) of CA and CTA-9, the C 1s spectrum of CTA-9 (b), the O 1s spectra of CA and CTA-9 (c), the Fe 2p spectrum of CTA-9 (d), the Ti 2p spectrum of CTA-9 (e).

$2p_{1/2}$ of TiO_2, respectively. The O 1s spectrum of CTA-9 (Fig. 3e) was deconvoluted into three peaks located at 529.8, 531.1 and 532.9 eV, which can be ascribed to the lattice oxygen of TiO_2 and β-FeOOH, the adsorbed oxygen and C–O, respectively. The peak of C–O was observed to shift to higher binding energies, implying the C–O group of CTA-9 has a strong interaction with TiO_2 and β-FeOOH.

SEM images of CTA-9 (Fig. 4a) show β-FeOOH NPs were uniformly distributed on the aerogel surface.[26] The EDS mappings (Fig. 4b) reveal the uniform distribution of Ti and Fe elements, and the distribution of Fe was similar to Ti. TEM images of CTA-9 are shown in Fig. 4c. As seen in Fig. 4c, the

morphology of β-FeOOH was observed to be spindle rod shaped, which is typical for β-FeOOH. Moreover, a compact incorporation of β-FeOOH and TiO_2 was observed, explaining the similar distribution of Fe and Ti elements in the energy spectrum, which facilitates the transfer of photogenerated electrons. These results reveal β-FeOOH NPs and TiO_2 particles successfully synthesized and fully contacted with each other, which would improve the photocatalytic efficiency of composite aerogels.

3.2 Photocatalytic activity of composite

The photo-Fenton degradation activities of β-FeOOH/TiO_2/cellulose nanocomposite aerogels were evaluated by degradation of MB under weak UV irradiation. Fig. 5a shows the degradation ability of composite aerogels with different content of β-FeOOH. The photocatalytic degradation efficiency of CTA was higher than that of CT and CA-9, which means there is synergy between TiO_2 and β-FeOOH to enhance degradation efficiency. From the TG results (Fig. 5c), the amount of β-FeOOH in CTA-6, CTA-9 and CTA-12 were calculated to be 7.8 wt%, 13.5 wt% and 15.7 wt%, respectively. Among the above three compositions of CTA, CTA-9 show the highest degradation activity *via* photo-Fenton reaction, achieving a removal ratio of 97.2% in 65 min. The degradation rate constants (k) for CTA-6, CTA-9 and CTA-12 were 0.045 min^{-1}, 0.053 min^{-1} and 0.039 min^{-1}, respectively (Fig. 5b). It is observed that the photocatalytic activity of CTA increases first and then decreases with the increase of β-FeOOH content. Excessive β-FeOOH NPs loaded in the cellulose aerogel resulted in a denser network, which has an adverse effect on internal mass transfer and photocatalytic activity. In addition to the amount of loaded
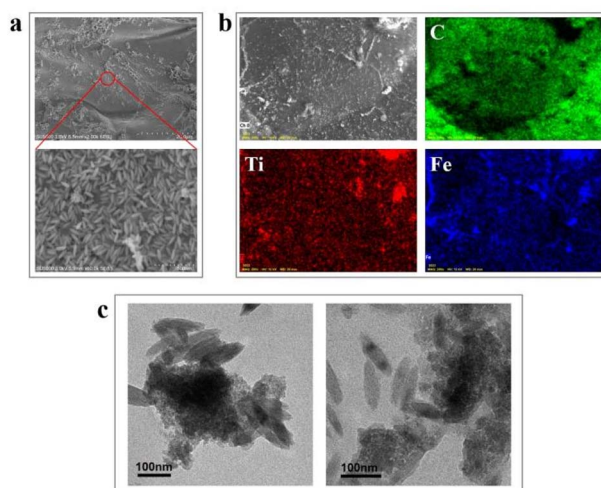

Fig. 4 SEM images of CTA-9 (a), EDS mappings of CTA-9 element distribution (b) and TEM images of CTA-9 (c).
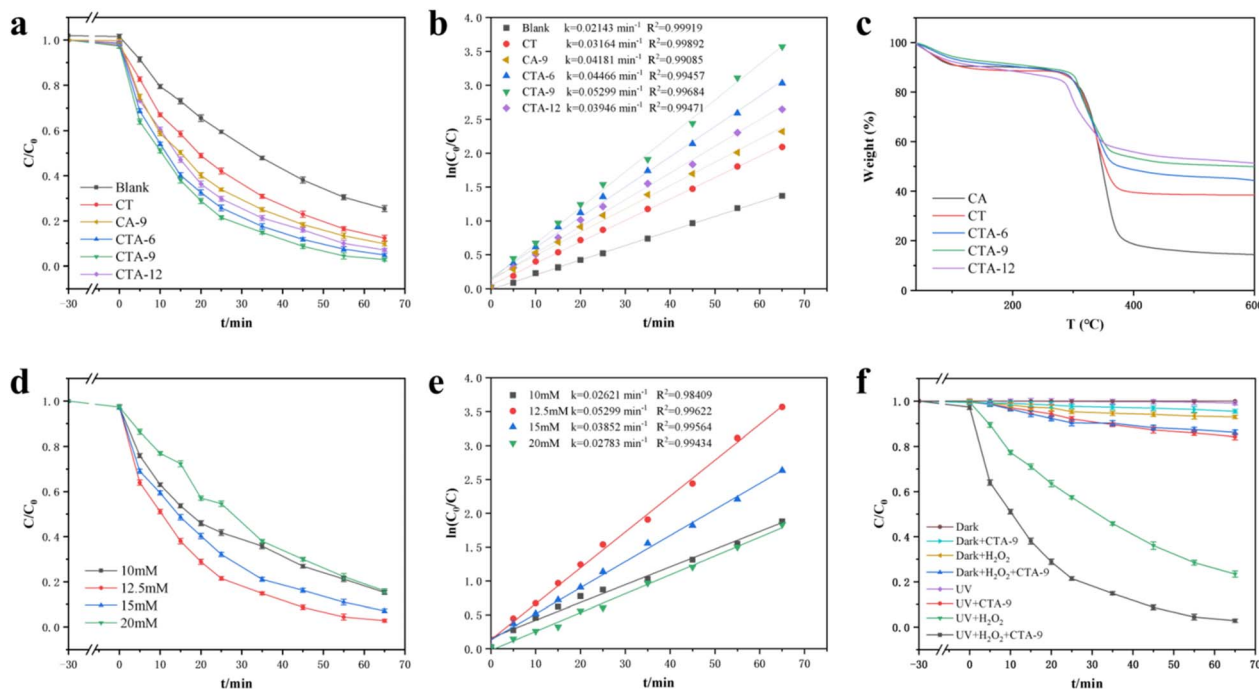
Fig. 5 (a) Comparison of MB removal among different photocatalysts ($c_0 = 20$ mg L^{-1}, pH = 3, 12.5 mM H_2O_2). (b) A plot of $\ln(c_0/c)$ *versus* irradiation time for degradation of MB at different photocatalysts. (c) DTG curves of cellulose composite aerogels. (d) Effect of initial H_2O_2 concentration on photo-Fenton reaction by CTA-9 ($c_0 = 20$ mg L^{-1}, pH = 3). (e) A plot of $\ln(c_0/c)$ *versus* irradiation time for degradation of MB at different concentration of H_2O_2. (f) Degradation of MB for various degradation process ($c_0 = 20$ mg L^{-1}, pH = 3, 12.5 mM H_2O_2).

catalyst, H_2O_2 concentration also is an important factor in determining the efficiency of the photo-Fenton reaction.

The photocatalytic performance of CTA-9 was studied at different H_2O_2 concentrations ranging from 10 mM to 20 mM (Fig. 5d). After 65 min of irradiation, the degradation rate of MB reached 84.7%, 97.2%, 92.8% and 84.0% at H_2O_2 concentration of 10, 12.5 15 and 20 mM, respectively. Meanwhile, the k values for the MB degradation were 0.026, 0.053, 0.039 and 0.029 min^{-1}, respectively (Fig. 5e). It is obvious that the degradation efficiency of MB increases as the concentration of H_2O_2 increased from 10 mM to 12.5 mM then decreased as the concentration above 12.5 mM. The increase of H_2O_2 concentration can increase the generation rate of hydroxyl radical concentration. However, the hydroxyl radical scavenging effect becomes more obvious at higher H_2O_2 concentration, which decrease the amount of available hydroxyl radical resulting in reduced degradation efficiency.[27,28] On the basis of these results, the 12.5 mM H_2O_2 concentration was chosen as the standard for subsequent experiments.

Fig. 5f compares the contribution of CTA-9, weak UV irradiation and H_2O_2 to MB degradation. First, there is negligible degradation of MB in the dark without catalyst and oxidant. In the presence of CTA-9 (without H_2O_2), the removal ratio of MB was only 4.5% in the dark after 65 min, while the ratio was increased to be 15.8% with the weak UV irradiation by the photocatalysis of CTA-9. Under dark and H_2O_2 condition, the degradation rates of 7.0% and 13.8% were obtained without and with CTA-9, respectively, and the increase is probably due to the adsorption of CTA-9 and the Fenton reaction occurring. Under

weak UV irradiation, in the presence of CTA-9 and H_2O_2, the degradation of MB rises up to 97.2% *via* photo-Fenton reaction, indicating that the synergistic effect of Fenton and photocatalysis was critical in increasing photocatalytic activity.[29,30] As shown in Table 1, compared with other heterogeneous photocatalysts and photo-Fenton catalysts, CTA-9 in this study can degrade MB dye faster at lower UV irradiation intensity, showing excellent photo-Fenton degradation catalytic performance.

The stability and reusability of catalysts is one of the important criteria for the potential in the practical application. The aerogel supported catalysts were easier to separate and recover as compared to the conventional powdery catalysts. To evaluate its stability of the photodegradation performance, the cyclic photodegradation were carried out for 5 times. As shown in Fig. 6, the removal ratio of degradation still retained 96.1% in 65 min after five cycles, indicating the excellent stability and recyclability of CTA-9. Catalyst particles were firmly anchored in the cellulose aerogel support with a continuous network structure by *in situ* synthesis, which effectively avoids the instability of catalyst during degradation. The excellent stability of the photodegradation performance of CTA-9 is due to this unique structure design.

3.3 Possible photocatalytic mechanism

Fig. 7a shows the UV-vis diffuse-reflectance spectrum of CT, CA-9 and CTA-9. The CT had a broad intense adsorption in the ultraviolet region. Meanwhile, the optical absorption edge of

Table 1 Comparison with other photocatalytic and photo-Fenton catalyst

Catalyst	Dye	Degradation (%)	Time (min)	Irradiation source and power	Degradation style	Ref.
TiO$_2$-wrapped cotton nanofiber	MB	90	180	1000 W UV lamp	Photocatalytic degradation	31
TiO$_2$@cellulose acetate	MB	90	120	300 W UV lamp	Photocatalytic degradation	32
Ag–Fe$_3$O$_4$/graphene composites	MB	99	120	40 W × 2 UV lamps	Photo-Fenton degradation	33
Fe$_3$O$_4$-natural iron ore/calcium alginate beads	Novacron blue (NB)	80	120	16 W UV lamp	Photo-Fenton degradation	34
β-FeOOH/TiO$_2$/cellulose nanocomposite aerogel	MB	97.2	65	6 W × 3 weak UV lamps	Photo-Fenton degradation	This work
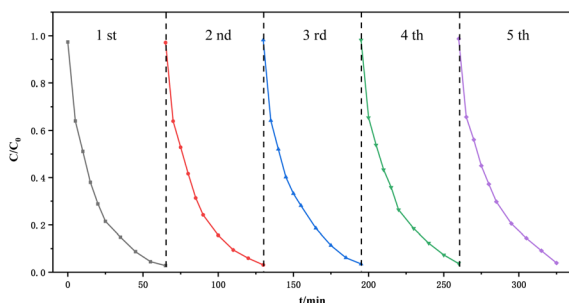
Fig. 6 The recyclability of CTA-9 in five cycles ($c_0 = 20$ mg L^{-1}, pH = 3, 12.5 mM H$_2$O$_2$).

CTA-9 was extended to the broader visible light region than CT and CA-9, which indicated the synergistic effect of TiO$_2$ and β-FeOOH to enhance the efficiency of light energy utilization. The band gap energy of theses samples could be estimated by the following equation:

$$(\alpha h\nu)^2 = B(h\nu - E_g)$$

where α, h, ν, B and E_g are absorption coefficient, Planck-constant, frequency, constant and the band gap width of semiconductor, respectively.[9,35]

The estimated E_g values for CT and CA-9 were 3.65 eV and 2.93 eV due to amorphous TiO$_2$ and β-FeOOH (Fig. 7b). In comparison with CT and CA-9, CTA-9 has a narrower band gap
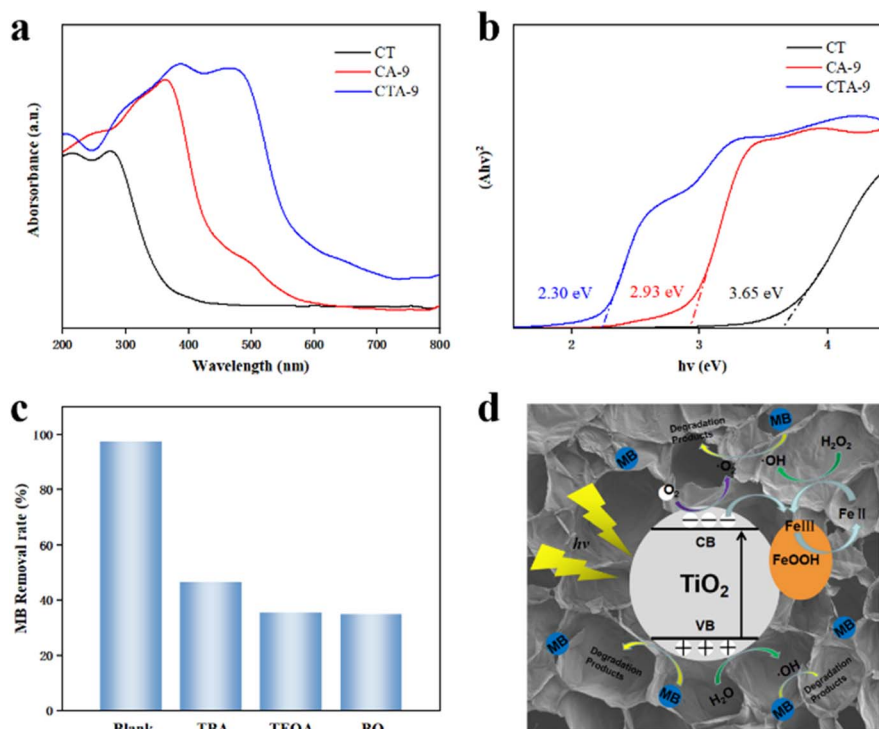

Fig. 7 (a) UV-vis diffuse-reflectance spectrum of the composite aerogels. (b) Plot of $(\alpha h\nu)^2$ versus $h\nu$ of the composite aerogels. (c) Effect of different reactive species scavengers in the CTA-9 photo-Fenton system. (d) Proposed mechanism for the photo-Fenton degradation of MB by β-FeOOH/TiO$_2$/cellulose nanocomposite aerogel.

(2.30 eV). This result indicates that the successful combination of TiO_2 and β-FeOOH extends the photo-absorption into visible light and narrows the band gap, consequently improving the photocatalytic performance of CTA-9.

In order to further elucidate the mechanism of photo-Fenton process, the radical trapping experiment was performed to detect the main active species. In this work, *tert*-butanol (TBA), triethanolamine (TEOA) and benzoquinone (BQ) were used as scavengers of hydroxyl radical ($^{\bullet}OH$), hole (h^+) and superoxide radical ($^{\bullet}O_2^-$), respectively. As shown in Fig. 7c, the removal efficiency of MB decreases from 97.2% to 46.3%, 35.2% and 34.9% after adding a certain amount of TBA, TEOA and BQ, implying that the three kinds of active species were involved in this photo-Fenton process. And h^+ and $^{\bullet}O_2^-$ were the most critical species and $^{\bullet}OH$ was secondary active species.

Based on the above results, the mechanism of β-FeOOH/TiO_2/cellulose nanocomposite aerogel photo-Fenton degradation of MB was proposed and illustrated in Fig. 7d. Under weak UV irradiation, the electrons of TiO_2 were excited from the valence band to the conduction band and electron–hole pairs were generated. Some of the photogenerated electrons of TiO_2 were transferred to the β-FeOOH, and the other photogenerated electrons would generate $^{\bullet}O_2^-$ by interacting with dissolved oxygen, which inhibited electron–hole recombination. These holes (h^+) of TiO_2 can oxidize H_2O to produce $^{\bullet}OH$ and also directly degrade MB. The electrons from TiO_2 can accelerate the transformation between Fe(III) and Fe(II), and Fe(II) can react with H_2O_2 to produce $^{\bullet}OH$. Thus, the combination between TiO_2 and β-FeOOH is conductive to producing more radicals and improving the hole oxidation capacity. Furthermore, cellulose aerogel not only can provide MB adsorption sites that can increase the contact rate between the dye and TiO_2/FeOOH particles to improve degradation efficiency, but also acted as a supporting material to prevent aggregation of particles and improve the stability and reusable performance of catalyst. Obviously, there was synergy between the individual components to improve the composite aerogel catalytic performance.

4. Conclusions

In summary, β-FeOOH/TiO_2/cellulose nanocomposite aerogels with excellent catalytic performance were successfully fabricated for photo-Fenton degradation of recalcitrant pollutants. The TiO_2 was grown *in situ* on precursor of cellulose hydrogel, and then β-FeOOH NPs were synthesized and fastened *in situ* on the composited gel. The synergistic effect between TiO_2 and β-FeOOH contributed to enhancing degradation efficiency, and the 3D framework of cellulose aerogel leads to the high catalytic stability and recyclability. CTA-9 exhibited high photocatalytic performance, and its removal efficiency of MB reached 97.2% under weak UV light for 65 min. In addition, the catalytic degradation performance of CTA-9 did not decrease obviously after 5 cycles, indicating the excellent stability and recyclability of CTA-9. Overall, this work provides a novel strategy for the preparation of efficient green heterogeneous catalyst by using renewable resources, and the composite catalyst has great potential for application in wastewater treatment.

Author contributions

Jun Jing: conceptualization, validation, writing – original draft, visualization; Yucheng Feng: methodology, software; Shuying Wu: writing – review & editing; Zhangjie Ye, Liu Yang, Jiaolong Li, Youyan Chen: methodology, software; Fei Yang: supervision, resources, writing – review & editing, funding acquisition.

Conflicts of interest

There are no conflicts to declare.

Acknowledgements

References

1 S. Khan, M. Naushad, M. Govarthanan, J. Iqbal and S. M. Alfadul, *Environ. Res.*, 2022, **207**, 112609.

2 A. Tkaczyk, K. Mitrowska and A. Posyniak, *Sci. Total Environ.*, 2020, **717**, 137222.

3 S. Kim, S.-N. Nam, A. Jang, M. Jang, C. M. Park, A. Son, N. Her, J. Heo and Y. Yoon, *Chemosphere*, 2022, **286**, 131916.

4 Y. He, Z. Wang, T. Li, X. Peng, Y. Tang and X. Jia, *Chemosphere*, 2022, **308**, 136443.

5 M. Hassan, R. Naidu, J. H. Du, Y. J. Liu and F. J. Qi, *Sci. Total Environ.*, 2020, **702**, 134893.

6 R. Ameta, A. K. Chohadia, A. Jain and P. B. Punjabi, in *Advanced Oxidation Processes for Waste Water Treatment*, ed. S. C. Ameta and R. Ameta, Academic Press, 2018, pp. 49–87, DOI: **10.1016/B978-0-12-810499-6.00003-6**.

7 M.-h. Zhang, H. Dong, L. Zhao, D.-x. Wang and D. Meng, *Sci. Total Environ.*, 2019, **670**, 110–121.

8 F. Xiao, W. Li, L. Fang and D. Wang, *J. Hazard. Mater.*, 2016, **308**, 11–20.

9 C. Zhang, H.-C. Yang, L.-S. Wan, H.-Q. Liang, H. Li and Z.-K. Xu, *ACS Appl. Mater. Interfaces*, 2015, **7**, 11567–11574.

10 L. Zhang, N. Yang, Y. Han, X. Wang, L. Zhang, Y. Sun and B. Jiang, *Sep. Purif. Technol.*, 2021, **279**, 119684.

11 S. Mortazavi-Derazkola, M. Salavati-Niasari, O. Amiri and A. Abbasi, *J. Energy Chem.*, 2017, **26**, 17–23.

12 S. He, C. Yan, X.-Z. Chen, Z. Wang, T. Ouyang, M.-L. Guo and Z.-Q. Liu, *Appl. Catal., B*, 2020, **276**, 119138.

13 Q. Li, H. Kong, P. Li, J. Shao and Y. He, *J. Hazard. Mater.*, 2019, **373**, 437–446.

14 J. Wang, L. Jiang, F. Liu, M. Jia, M. Liu, J. Li and Y. Lai, *Chem. Eng. J.*, 2021, **407**, 127195.

15 L. Li, C. Guo, J. Ning, Y. Zhong, D. Chen and Y. Hu, *Appl. Catal., B*, 2021, **293**, 120203.

16 T. T. N. Phan, A. N. Nikoloski, P. A. Bahri and D. Li, *RSC Adv.*, 2018, **8**, 36181–36190.

17 H. Long, A. Harley-Trochimczyk, T. Pham, Z. Tang, T. Shi, A. Zettl, C. Carraro, M. A. Worsley and R. Maboudian, *Adv. Funct. Mater.*, 2016, **26**, 5158–5165.

18 Z.-J. Li, Z.-W. Huang, W.-L. Guo, L. Wang, L.-R. Zheng, Z.-F. Chai and W.-Q. Shi, *Environ. Sci. Technol.*, 2017, **51**, 5666–5674.

19 M. Hasanpour, S. Motahari, D. Jing and M. Hatami, *Chemosphere*, 2021, **284**, 131320.

20 X. Su, Q. Liao, L. Liu, R. Meng, Z. Qian, H. Gao and J. Yao, *Cellulose*, 2017, **24**, 1017–1029.

21 F. Sun, D. Xu, Y. Xie, F. Liu, W. Wang, H. Shao, Q. Ma, H. Yu, W. Yu and X. Dong, *J. Colloid Interface Sci.*, 2022, **628**, 614–626.

22 X. Zhang, Y. Feng, D. Gao, W. Ma, C. Jin, X. Jiang, J. Lin and F. Yang, *Carbohydr. Polym.*, 2022, **282**, 119136.

23 Y. Tian, M. Wu, R. Liu, D. Wang, X. Lin, W. Liu, L. Ma, Y. Li and Y. Huang, *J. Hazard. Mater.*, 2011, **185**, 93–100.

24 S. Music, S. Krehula, S. Popovic and Z. Skoko, *Mater. Lett.*, 2003, **57**, 1096–1102.

25 M. Wang, Z. Xu, Y. Hou, P. Li, H. Sun and Q. J. Niu, *Sep. Purif. Technol.*, 2020, **249**, 117159.

26 J. Yue, X. Jiang and A. Yu, *J. Nanopart. Res.*, 2011, **13**, 3961–3974.

27 X. Yang, W. Chen, J. Huang, Y. Zhou, Y. Zhu and C. Li, *Sci. Rep.*, 2015, **5**, 10632.

28 C. Wu and K. G. Linden, *Water Res.*, 2008, **42**, 4780–4790.

29 J. Wang, X. Li, Q. Cheng, F. Lv, C. Chang and L. Zhang, *Carbohydr. Polym.*, 2020, **229**, 115470.

30 X. Qian, Y. Wu, M. Kan, M. Fang, D. Yue, J. Zeng and Y. Zhao, *Appl. Catal., B*, 2018, **237**, 513–520.

31 L. Zhang, J. Wan, Z. Hu and W. Jiang, *BioResources*, 2017, **12**(3), 6062–6081.

32 S.-D. Wang, Q. Ma, H. Liu, K. Wang, L.-Z. Zhang and K.-Q. Zhang, *RSC Adv.*, 2015, **5**(51), 40521–40530.

33 R. Saleh and A. Taufik, *J. Environ. Chem. Eng.*, 2019, **7**(1), 102895.

34 S. Ben Ayed, L. Mansour, V. Vaiano, A. Halim Harrath, F. Ayari and L. Rizzo, *J. Photochem. Photobiol., A*, 2023, **438**, 114566.

35 C. Liu, H. Dai, C. Tan, Q. Pan, F. Hu and X. Peng, *Appl. Catal., B*, 2022, **310**, 121326.